The Sagnac effect: 100 years later / L'effet Sagnac : 100 ans après

Towards a solid-state ring laser gyroscope

Vers un gyrolaser à état solide

Noad El Badaoui [a,b], Bertrand Morbieu [a], Philippe Martin [b], Pierre Rouchon [b], Jean-Paul Pocholle [c], François Gutty [c], Gilles Feugnet [c], Sylvain Schwartz [c,*]

[a] *Thales Avionics, 40, rue de la Brelandière, BP 128, 86101 Châtellerault, France*
[b] *Centre Automatique et Systèmes, Mines ParisTech, PSL Research University, 60, boulevard Saint-Michel, 75272 Paris cedex 06, France*
[c] *Thales Research and Technology France, Campus Polytechnique, 1, avenue Augustin Fresnel, 91767 Palaiseau, France*

A R T I C L E   I N F O

A B S T R A C T

In this paper, we report our recent progress towards a solid-state ring laser gyroscope (RLG), where mode competition is circumvented by active control of differential losses, and nonlinear effects are mitigated by longitudinal vibration of the gain medium. The resulting dynamics is significantly different from that of a classical helium–neon RLG, owing in particular to parametric resonances that occur when the Sagnac frequency is an integer multiple of the crystal vibration frequency. We describe the main experimental and theoretical results obtained so far, and the prospects of practical applications in the near future.

Published by Elsevier Masson SAS on behalf of Académie des sciences.

R É S U M É

Nous décrivons dans cet article nos récents progrès vers la réalisation d'un gyrolaser à état solide. Dans ce dispositif, le problème de la compétition entre modes est résolu par un contrôle actif des pertes différentielles, et les effets non linéaires sont fortement atténués par la mise en vibration du milieu à gain. La dynamique d'un tel système est significativement différente de celle d'un gyrolaser à hélium–néon classique, en particulier à cause des résonances paramétriques qui surviennent lorsque la fréquence Sagnac est un multiple entier de la fréquence de vibration du cristal. Nous décrivons les principaux résultats expérimentaux et théoriques obtenus jusqu'ici et discutons les perspectives d'applications pratiques à court et moyen termes.

Published by Elsevier Masson SAS on behalf of Académie des sciences.

1. Introduction

A century after Sagnac pioneering experiments [1,2] and more than fifty years after the first demonstration of a ring laser gyroscope by Macek and Davis [3], optical rotation sensing is still a remarkably active field of research. It includes integrated

---

* Corresponding author.
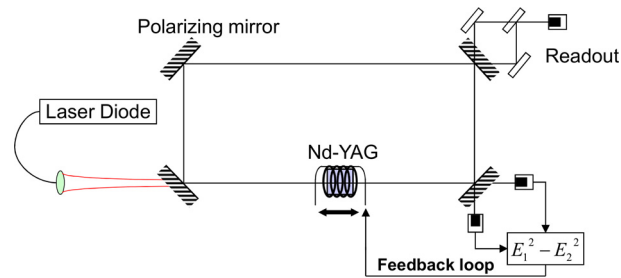*E-mail address:* sylvain.schwartz@thalesgroup.com (S. Schwartz).

Fig. 1. Basic principle of the solid-state ring laser gyroscope. The double arrow relates to the vibration of the Nd–YAG crystal, which will be discussed in Sections 3 and 4. (Color online.)

optics [4–6], slow and fast light [7–14], hollow core fibers [15–17] and large instruments for fundamental science [18–21]. From an industry perspective, two solutions have emerged and are routinely used for guidance, navigation and control: the ring laser gyroscope (RLG) [22] and the interferometric fiber-optic gyroscope (IFOG) [23]. Although the two devices can be shown to be equivalent in theory (in the sense that they have the same shot-noise limit for equal size and optical power, under the additional hypothesis that the number of fiber turns in the IFOG is equal to the finesse of the cavity in the RLG [24,14]), they differ by their practical implementation: the IFOG is shot-noise limited, but more sensitive to external perturbations (especially time-dependent temperature gradients [25]), while the RLG is more robust to its environment, but has an additional source of noise resulting from mechanical dither (which is the best known solution so far to circumvent the lock-in phenomenon [26,27]).

A key requirement common to all kinds of optical gyroscopes is reciprocity, which means that the two counter-propagating beams must share the same optical path, in order to make the variations of the latter common-mode. For the RLG, which is an active device, this implies that the two counter-propagating modes must also share the same gain medium, and are thus subject to mode competition, which tends to hinder bidirectional emission. This problem is classically solved by using a gaseous gain medium for the RLG, typically a helium–neon mixture. The trick is to tune the cavity out of resonance with the atoms at rest, such that the two counter-propagating modes are resonant, owing to the Doppler effect, with two different classes of atoms (corresponding to opposite classes of velocity), ensuring stable bidirectional emission. From a practical point of view, it would be a strong asset to be able to replace the gaseous mixture with a solid-state component, taking advantage of the recent progress in cost reduction, lifetime and reliability driven by markets much bigger than inertial sensing. In this case, however, the Doppler trick cannot be used anymore, and one has to implement new techniques to circumvent mode competition and nonlinear couplings.

In this manuscript, we report our recent progress towards the achievement of a diode-pumped neodymium-doped yttrium aluminium garnet (Nd–YAG) RLG. We will first describe the technique of active control of the differential losses that we have implemented on this device, enabling bidirectional emission and rotation sensing. We will then discuss the nonlinearity of the resulting frequency response curve, which is mostly due to the existence of a population inversion grating in the amplifying medium. Based on theoretical predictions from a semiclassical model and on experimental results, we will show how the grating can be washed out by vibrating the gain crystal along the laser axis, significantly improving the linearity of the frequency response. We will also describe the residual nonlinearities, due for the most part to a parametric resonance between the Sagnac frequency and the crystal vibration frequency. Finally, we will discuss the expected performance of this novel rotation sensor, and prospects for future applications.

2. Circumventing mode competition in the solid-state ring laser

Our basic setup is sketched in Fig. 1. It is made of a four-mirror ring cavity, containing a diode-pumped Nd–YAG crystal as the gain medium. The readout system combines the beams emitted from the two counter-propagating modes to form a beat signal on a photodiode.

The issue of mode competition is addressed by an active control of the differential losses between the counter-propagating modes [28–30]. The basic idea is to measure independently the intensity of the two beams, and to make the differential losses proportional to the intensity difference using a feedback loop, with the appropriate sign such that the more intense mode gets the higher losses at any time. In practice, the differential losses are created by polarization effects, based on the combination of a nonreciprocal rotation (obtained by Faraday effect in the YAG crystal placed inside a solenoid), a reciprocal rotation (obtained by a slight non-planarity of the cavity) and a polarizing effect (obtained by an appropriate coating on one of the mirrors). The amount of differential losses is proportional (in the limit of small rotations) to the current flowing in the solenoid, which is controlled by the feedback loop as described above.

The experimental frequency response curve of the solid-state ring laser with active stabilization of the differential losses is shown in Fig. 2. Below a critical rotation rate on the order of 10 deg/s, nonlinear couplings in the gain medium dominate and no stable signal is observed. Above this critical rotation rate, the feedback loop becomes efficient and a stable beat signal is obtained. As can be seen in Fig. 2, the frequency response curve of the solid-state RLG is nonlinear, with an upwards deviation from the ideal Sagnac line. The main reason for this nonlinearity is the presence of a population inversion grating
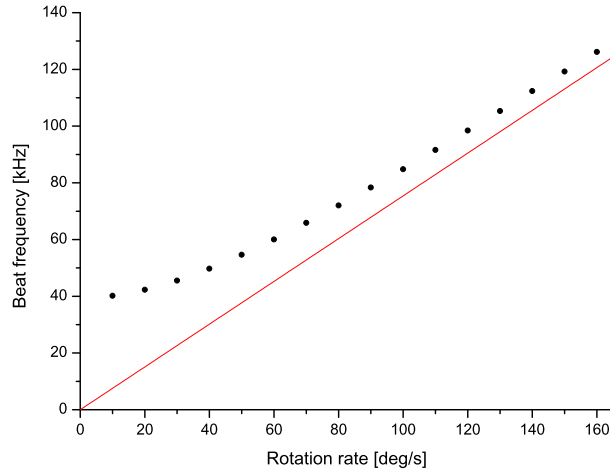
Fig. 2. Typical (experimental) frequency response of the solid-state ring laser gyroscope without crystal vibration. (Color online.)

in the gain medium [30], which couples the two counter-propagating modes. This grating results from the inhomogeneous saturation of the gain by the interfering counter-propagating modes. Its effect on the frequency response decreases for increasing rotation rates, because it becomes more and more difficult for the population inversion density, which has a finite response time (about 230 μs in our case), to follow the variations of the light pattern.

Based on the latter observation, we have introduced in the laser cavity a mechanical device to vibrate the gain crystal along the light propagation axis [31], with a view to washing out the population inversion grating. As will be discussed in the following, this can significantly improve the linearity of the frequency response curve at low rotation rates provided the appropriate choice of experimental parameters is made. This requires a careful description of the laser dynamics including crystal vibration [32], which will be presented in the next sections.

3. Semiclassical description of the solid-state RLG with crystal vibration

In order to describe the electric field inside the ring cavity, we assume that there is only one laser mode in each direction of propagation, something which is experimentally obtained owing to crystal vibration, which counteracts spatial hole burning effects [33,34]. We furthermore assume that the two modes have the same polarization state. This eventually leads, in the plane wave approximation, to the following expression for the electric field:

$$E(x, t) = \Re\left[\sum_{p=1}^{2} \tilde{E}_p(t) e^{i(\omega_c t + \mu_p kx)}\right]$$

where $\mu_p = (-1)^p$ and where ω_c and k are respectively the angular and spatial average frequencies of the laser, whose longitudinal axis is associated with the x coordinate. The dynamics of the solid-state RLG is then ruled, in the rotating wave approximation, by the following semiclassical equations [35]:

$$\frac{d\tilde{E}_{1,2}}{dt} = -\frac{\gamma_{1,2}}{2}\tilde{E}_{1,2} + i\frac{\tilde{m}_{1,2}}{2}\tilde{E}_{2,1} - i\mu_{1,2}\frac{\Omega}{2}\tilde{E}_{1,2} + \frac{\sigma}{2T}\left(\tilde{E}_{1,2}\int_0^l N_c \, dx + \tilde{E}_{2,1}e^{2ikx_c}\int_0^l N_c e^{-2i\mu_{1,2}kx} \, dx\right) \tag{1}$$

where $\gamma_{1,2}$ are the cavity losses associated with the counter-propagating modes, $\tilde{m}_{1,2}$ are the backscattering coefficients, Ω is the (angular) frequency difference between the counter-propagating modes, σ is the laser cross section, T is the cavity round-trip time, l is the size of the gain medium, N_c is the population inversion density in the frame of the vibrating crystal and x_c is the coordinate (in the laser frame) of a fixed point attached to the crystal, given by:

$$x_c = \frac{x_m}{2}\cos(2\pi f_m t) \tag{2}$$

where x_m is the amplitude of the movement and $f_m = \omega_m/(2\pi)$ its frequency. The backscattering coefficients, which depend on the spatial inhomogeneities of the propagation medium, have the following expression [35]:

$$\tilde{m}_{1,2}(t) = \tilde{m}_{1,2}^c e^{-2i\mu_{1,2}kx_c(t)} + \tilde{m}_{1,2}^m \tag{3}$$

where $\tilde{m}_{1,2}^c$ is the backscattering coefficient associated with the diffusion inside the YAG crystal, and $\tilde{m}_{1,2}^m$ is the backscattering coefficient associated with any other source of diffusion inside the laser cavity, essentially the mirrors. The stabilizing coupling described in the previous section is modelled (neglecting finite-bandwidth effects) by taking losses of the form:
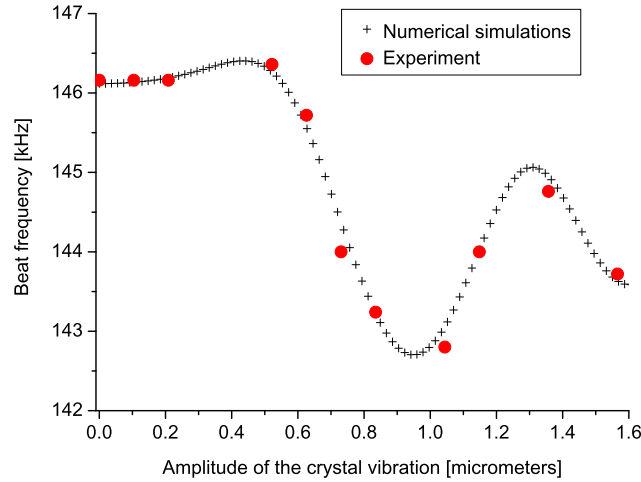
Fig. 3. Beat frequency as a function of the amplitude of the crystal movement for $\dot{\theta} = 200$ deg/s with the crystal vibrating at $f_m \simeq 40$ kHz. The experimental data (red circles) are in good agreement with numerical simulations (black crosses) obtained using the following measured parameters [38]: $\gamma = 15.34 \ 10^6 \ \text{s}^{-1}$, $\eta = 0.21$, $|\tilde{m}^c_{1,2}| = 1.5 \ 10^4 \ \text{s}^{-1}$, $|\tilde{m}^m_{1,2}| = 8.5 \ 10^4 \ \text{s}^{-1}$, $\arg(\tilde{m}^c_1/\tilde{m}^c_2) = \arg(\tilde{m}^m_1/\tilde{m}^m_2) = \pi/17$, $K = 10^7 \ \text{s}^{-1}$. Integration step is 0.1 μs, average values are computed between 8 and 10 ms. (Color online.)

$$\gamma_{1,2} = \gamma - \mu_{1,2} K a \big(|\tilde{E}_1|^2 - |\tilde{E}_2|^2 \big) \tag{4}$$

where γ is the average loss coefficient, $K > 0$ represents the strength of the stabilizing coupling and a is the saturation parameter. The population inversion density function in the frame of the vibrating crystal $N_c(x,t)$ is ruled by the following equation:

$$\frac{\partial N_c}{\partial t} = W_{\text{th}}(1 + \eta) - \frac{N_c}{T_1} - \frac{a N_c |\tilde{E}_1 e^{-ik(x+x_c)} + \tilde{E}_2 e^{ik(x+x_c)}|^2}{T_1} \tag{5}$$

where η is the relative excess of pumping power above the threshold value W_{th} and T_1 is the lifetime of the population inversion. The difference Ω between the eigenfrequencies of the counter-propagating modes is induced by the combined effects of rotation (Sagnac effect [36]) and crystal vibration (Fresnel–Fizeau drag effect [37]), resulting in the following expression:

$$\Omega = \Omega_s - \frac{4\pi \dot{x}_c(t) l_c(n^2 - 1)}{\lambda L} \tag{6}$$

where $\Omega_s = 8\pi A\dot{\theta}/(\lambda L)$ is the Sagnac angular frequency, A is the area enclosed by the ring cavity, L is the (optical) length of the cavity, $\dot{\theta}$ is the angular velocity of the cavity around its axis, $\lambda = 2\pi c/\omega_c$ is the emission wavelength, and l_c and n are respectively the length and the refractive index of the crystal. In Eq. (6), we have neglected the effect of dispersion in the YAG crystal, which is much smaller than the Fresnel–Fizeau drag effect in our case.

To summarize, the dynamics of the solid-state RLG with crystal vibration is described by Eqs. (1), in conjunction with Eqs. (2), (3), (4), (5) and (6). Of course, this model is too complex to be solved analytically. However, it can be integrated numerically with realistic laser parameters, providing a good agreement with the experimental results. This is illustrated by the data shown in Fig. 3, where the beat frequency is plotted as a function of the amplitude of the crystal vibration x_m for $f_m \simeq 40$ kHz. The experimental frequency response curve has in this case a non-trivial shape, which is well reproduced by the numerical simulation.

4. Dynamics of the solid-state RLG with high-frequency crystal vibration

The linearity of the solid-state RLG can be significantly improved by making the crystal vibration frequency ω_m much bigger than all other frequencies involved in the laser dynamics, namely $|\Omega_s|$, $|\tilde{m}^m_{1,2}|$, $|\tilde{m}^c_{1,2}|$ and the relaxation frequency $\omega_r = \sqrt{\gamma \eta/T_1}$ [35], as will be discussed in this section.

4.1. Analytical derivation of the beat frequency in the limit of high rotation rates

In this subsection, we furthermore assume that the rotation rate is high enough for the following conditions to be fulfilled:

$$\omega_m > |\Omega_s| \gg |\tilde{m}^m_{1,2}|, |\tilde{m}^c_{1,2}|, \omega_r \tag{7}$$

In this case, the nonlinearity of the frequency response of the solid-state RLG can be analytically estimated. To do so, we first introduce N_0 and N_1, respectively the mean and first spatial harmonics of the population inversion density function $N_c(x, t)$, defined by:

$$N_0 = \frac{1}{l} \int_0^l N_c(x, t)\, dx \quad \text{and} \quad N_1 = \frac{1}{l} \int_0^l N_c(x, t) e^{2ikx}\, dx$$

If we furthermore assume that the pumping rate is close to the threshold value (i.e. $\eta \ll 1$), then we can rewrite Eqs. (1) and (5) as follows:

$$\begin{cases} \dfrac{d\tilde{E}_{1,2}}{dt} = \left(\dfrac{Z}{2}N_0 - \dfrac{\gamma_{1,2}}{2}\right)\tilde{E}_{1,2} + \dfrac{i\tilde{m}_{1,2}}{2}\tilde{E}_{2,1} - \dfrac{i\mu_{1,2}\Omega}{2}\tilde{E}_{1,2} + \dfrac{Z}{2}N_{1,2}e^{-2i\mu_{1,2}kx_c}\tilde{E}_{2,1} \\[2mm] \dfrac{dN_0}{dt} = W_{th}(1+\eta) - \dfrac{N_0}{T_1} - \dfrac{a}{2T_1}N_{th}\left(|\tilde{E}_1|^2 + |\tilde{E}_2|^2\right) \\[2mm] \dfrac{dN_1}{dt} = -\dfrac{N_1}{T_1} - \dfrac{a}{2T_1}N_{th}e^{-2ikx_c}\tilde{E}_1\tilde{E}_2^* \end{cases} \tag{8}$$

where $Z = \sigma l/T$, $N_2 = N_1^*$ and N_{th} is the value of N_0 at the laser threshold. It obeys the following relation:

$$W_{th} = \frac{N_{th}}{T_1} \simeq \frac{\gamma}{ZT_1} \tag{9}$$

where the contribution of backscattering has been neglected in the expression of N_{th}. We will now derive an approximation of this system using the mathematical theory of averaging over nonlinear dynamical systems [39,40]. For simplicity, we neglect the Fresnel–Fizeau term introduced in Eq. (6), such that $\Omega = \Omega_s$. Going into the rotating frame by setting:

$$\tilde{E}_1 = e^{i\Omega_s t/2}F_1 \quad \text{and} \quad \tilde{E}_2 = e^{-i\Omega_s t/2}F_2 \tag{10}$$

the system (8) becomes:

$$\begin{cases} \dfrac{dF_{1,2}}{dt} = \left(\dfrac{Z}{2}N_0 - \dfrac{\gamma_{1,2}}{2}\right)F_{1,2} + \dfrac{Z}{2}N_{1,2}e^{-i\mu_{1,2}kx_m\cos(\omega_m t)}e^{i\mu_{1,2}\Omega_s t}F_{2,1} + \dfrac{i}{2}\left[\tilde{m}_{1,2}^m + \tilde{m}_{1,2}^c e^{-i\mu_{1,2}kx_m\cos(\omega_m t)}\right]e^{i\mu_{1,2}\Omega_s t}F_{2,1} \\[2mm] \dfrac{dN_0}{dt} = W_{th}(1+\eta) - \dfrac{N_0}{T_1} - \dfrac{a}{2T_1}N_{th}\left(|F_1|^2 + |F_2|^2\right) \\[2mm] \dfrac{dN_1}{dt} = -\dfrac{N_1}{T_1} - \dfrac{a}{2T_1}N_{th}e^{-ikx_m\cos(\omega_m t)}e^{i\Omega_s t}F_1 F_2^* \end{cases}$$

Using the classical series involving the Bessel functions J_n:

$$e^{ikx_m\cos(\omega_m t)} = J_0(kx_m) + \sum_{n=1}^{+\infty} i^n J_n(kx_m)\left(e^{in\omega_m t} + e^{-in\omega_m t}\right)$$

we can perform a first order averaging of the previous system of equations considering the fact that the frequencies $n\omega_m \pm \Omega_s$ are much larger than the other frequencies involved in the laser dynamics (see (7)). This provides the following model:

$$\begin{cases} \dfrac{d\bar{F}_{1,2}}{dt} = \left(\dfrac{Z}{2}\bar{N}_0 - \dfrac{\bar{\gamma}_{1,2}}{2}\right)\bar{F}_{1,2} \\[2mm] \dfrac{d\bar{N}_0}{dt} = W - \dfrac{\bar{N}_0}{T_1} - \dfrac{a}{2T_1}N_{th}\left(|\bar{F}_1|^2 + |\bar{F}_2|^2\right) \\[2mm] \dfrac{d\bar{N}_1}{dt} = -\dfrac{\bar{N}_1}{T_1} \end{cases} \tag{11}$$

leading to the following equilibrium values for the averaged parameters:

$$\bar{\gamma}_1 = \bar{\gamma}_2 = \gamma, \qquad a|F_1|^2 = a|F_2|^2 = \eta, \qquad \bar{N}_0 = \gamma/Z \quad \text{and} \quad \bar{N}_1 = 0 \tag{12}$$

Let us compute the second order correction for $(\bar{F}_1, \bar{F}_2, \bar{N}_0, \bar{N}_1)$ around the equilibrium of (11). The small fluctuations denoted with a δ around the average values (denoted with a bar) admit the following form:
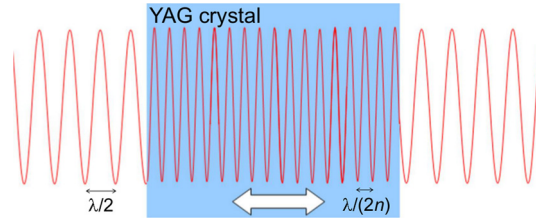
Fig. 4. Sketch of the optical standing wave inside and outside the YAG crystal. When the crystal is physically translated by $\lambda/2$, the relative position between the optical standing wave and a fixed point in the crystal is changed by $\lambda/(2n)$. (Color online.)

$$\delta F_1 = \frac{1}{2}\left[-\frac{\tilde{m}_1{}^{\mathrm{m}} + \tilde{m}_1{}^{\mathrm{c}} J_0(kx_{\mathrm{m}})}{\Omega_{\mathrm{s}}} + i\tilde{m}_1{}^{\mathrm{c}} J_1(kx_{\mathrm{m}})\left(\frac{e^{i\omega_{\mathrm{m}}t}}{\omega_{\mathrm{m}} - \Omega_{\mathrm{s}}} - \frac{e^{-i\omega_{\mathrm{m}}t}}{\omega_{\mathrm{m}} + \Omega_{\mathrm{s}}}\right)\right]e^{-i\Omega_{\mathrm{s}}t}\bar{F}_2$$

$$\delta F_2 = \frac{1}{2}\left[\frac{\tilde{m}_2{}^{\mathrm{m}} + \tilde{m}_2{}^{\mathrm{c}} J_0(kx_{\mathrm{m}})}{\Omega_{\mathrm{s}}} - i\tilde{m}_2{}^{\mathrm{c}} J_1(kx_{\mathrm{m}})\left(\frac{e^{i\omega_{\mathrm{m}}t}}{\omega_{\mathrm{m}} + \Omega_{\mathrm{s}}} - \frac{e^{-i\omega_{\mathrm{m}}t}}{\omega_{\mathrm{m}} - \Omega_{\mathrm{s}}}\right)\right]e^{i\Omega_{\mathrm{s}}t}\bar{F}_1$$

$$\delta N_0 = 0$$

$$\delta N_1 = i\frac{a\gamma}{2ZT_1}\left[\frac{J_0(kx_{\mathrm{m}})}{\Omega_{\mathrm{s}}} - iJ_1(kx_{\mathrm{m}})\left(\frac{e^{i\omega_{\mathrm{m}}t}}{\omega_{\mathrm{m}} + \Omega_{\mathrm{s}}} - \frac{e^{-i\omega_{\mathrm{m}}t}}{\omega_{\mathrm{m}} - \Omega_{\mathrm{s}}}\right)\right]e^{i\Omega_{\mathrm{s}}t}\bar{F}_1\bar{F}_2^*$$

where we have neglected the J_n terms with $n \geq 2$ for simplicity. In order to compute the second-order approximation, we replace (F_1, F_2, N_0, N_1) by their first-order value $(\bar{F}_1 + \delta F_1, \bar{F}_2 + \delta F_2, \bar{N}_0 + \delta N_0, \bar{N}_1 + \delta N_1)$ in the second members of differential equations (11), and re-average the fast-oscillating terms. The second order approximation eventually leads to:

$$\frac{d\bar{F}_{1,2}}{dt} = \left(\frac{Z\bar{N}_0 - \bar{\gamma}_{1,2}}{2} + i\Delta_{1,2}\right)\bar{F}_{1,2} \tag{13}$$

where:

$$\Delta_1 - \Delta_2 = \frac{\gamma\eta}{2T_1}\left[\frac{J_0^2(kx_{\mathrm{m}})}{\Omega_{\mathrm{s}}} + \frac{2\Omega_{\mathrm{s}} J_1^2(kx_{\mathrm{m}})}{\Omega_{\mathrm{s}}^2 - \omega_{\mathrm{m}}^2}\right] + \frac{\tilde{m}_1{}^{\mathrm{c}}\tilde{m}_2{}^{\mathrm{c}}}{2\Omega_{\mathrm{s}}}J_0^2(kx_{\mathrm{m}}) + \frac{\tilde{m}_1{}^{\mathrm{m}}\tilde{m}_2{}^{\mathrm{m}}}{2\Omega_{\mathrm{s}}}$$

$$+ \frac{\tilde{m}_1{}^{\mathrm{c}}\tilde{m}_2{}^{\mathrm{m}} + \tilde{m}_1{}^{\mathrm{m}}\tilde{m}_2{}^{\mathrm{c}}}{2\Omega_{\mathrm{s}}}J_0(kx_{\mathrm{m}}) + \frac{\tilde{m}_1{}^{\mathrm{c}}\tilde{m}_2{}^{\mathrm{c}}\Omega_{\mathrm{s}} J_1^2(kx_{\mathrm{m}})}{\Omega_{\mathrm{s}}^2 - \omega_{\mathrm{m}}^2} \tag{14}$$

The measured (angular) beat frequency Ω_{beat} is defined in this formalism by the time average of $\arg(\tilde{E}_1/\tilde{E}_2)$. Based on Eqs. (10) and (13), it is equal to $\Omega_{\mathrm{beat}} = \Omega_{\mathrm{s}} + \Re(\Delta_1 - \Delta_2)$, where $\Delta_1 - \Delta_2$ is given by Eq. (14).

4.2. Physical interpretation and comparison with experiment

In a first approximation, we neglect the J_1 terms and keep only the dominant backscattering term $\tilde{m}_1{}^{\mathrm{c}}\tilde{m}_2{}^{\mathrm{c}}$ in Eq. (14), leading to:

$$\Omega_{\mathrm{beat}} \simeq \Omega_{\mathrm{s}} + \frac{\gamma\eta}{2\Omega_{\mathrm{s}}T_1}J_0^2(kx_{\mathrm{m}}) + \frac{\Re(\tilde{m}_1{}^{\mathrm{c}}\tilde{m}_2{}^{\mathrm{c}})}{2\Omega_{\mathrm{s}}}J_0^2(kx_{\mathrm{m}}) \tag{15}$$

Physically, the first correcting term is due to the residual effect of the population inversion grating, which goes to zero either for very high rotation rates or for a set of discrete values of the vibration amplitude corresponding to $J_0(kx_{\mathrm{m}}) = 0$. The second correcting term, resulting from backscattering in the crystal, is also reduced by crystal vibration, owing to the Doppler effect, which makes the backscattered light from one mode non-resonant anymore with the counter-propagating mode. The two effects go simultaneously to zero when $J_0(kx_{\mathrm{m}}) = 0$, corresponding to the situation where all the ions of the gain medium see on average the same intensity. The smallest value of x_{m} for which this happens is $kx_{\mathrm{m}} \simeq 2.405$, where $k = 2\pi/\lambda$ is the wavevector outside the YAG crystal, and shall not be confused in this context with its counterpart inside the YAG crystal $k_{\mathrm{c}} = n2\pi/\lambda$, as illustrated in Fig. 4. With $\lambda = 1.064$ μm, this leads to the following requirement on the vibration amplitude: $x_{\mathrm{m}} \simeq 0.41$ μm, which we typically achieve in practice using a resonant mechanical device excited by a piezoelectric ceramic.

The J_0^2 shape of the frequency response curve predicted in Eq. (15) is experimentally observed in Fig. 5, where the beat frequency is measured as a function of the amplitude of the crystal vibration for a fixed rotation rate of 55 deg/s and a crystal vibration frequency of $f_{\mathrm{m}} \simeq 168$ kHz. This curve provides an experimental signal to tune the vibration amplitude such that $J_0(kx_{\mathrm{m}}) = 0$.

When the latter condition is fulfilled, the frequency response curve of the solid-state RLG gets much closer to the ideal Sagnac line for $|\Omega_{\mathrm{s}}| \ll \omega_{\mathrm{m}}$, as illustrated in Fig. 6. Conversely, when the Sagnac frequency approaches the crystal
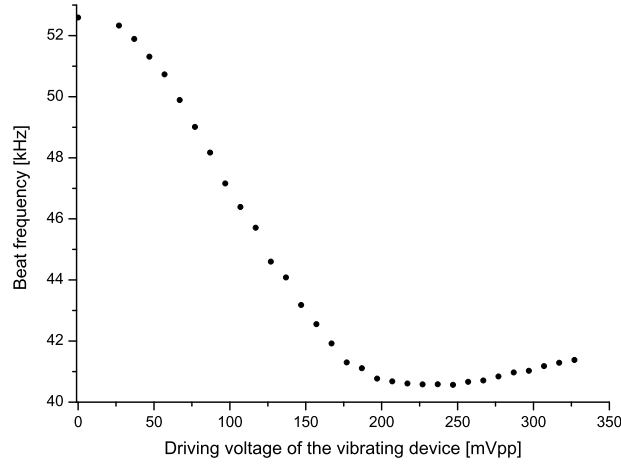
Fig. 5. Measured beat frequency as a function of the driving voltage of the vibrating device for $\dot{\theta} = 55$ deg/s, with the crystal vibrating at $f_m \simeq 168$ kHz. The driving voltage is proportional to the amplitude of the vibration up to $\simeq 250$ mV peak-to-peak (beyond this point, saturation occurs). The point where the curve is minimum corresponds to $J_0(kx_m) = 0$, hence $x_m \simeq 0.41$ μm.
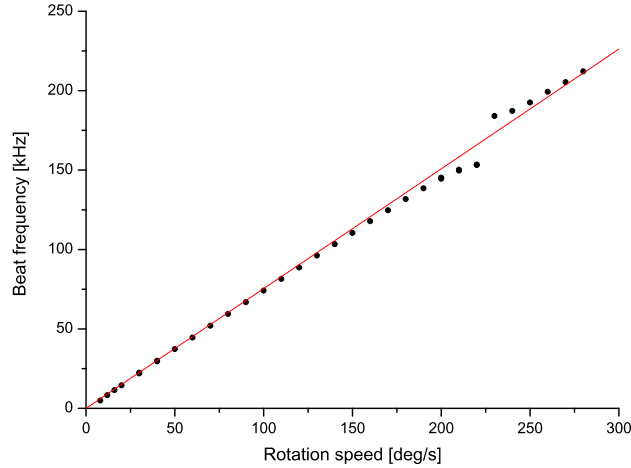

Fig. 6. Experimental frequency response of the solid-state ring laser gyroscope with $J_0(kx_m) = 0$ and $f_m \simeq 168$ kHz. A phenomenon of parametric resonance is observed when the Sagnac frequency approaches the crystal vibration frequency. (Color online.)

vibration frequency, the nonlinearity of the frequency response significantly increases. To give a quantitative estimate of this parametric resonance phenomenon, we include the J_1 terms in Eq. (14) while setting the J_0 terms to zero, leading to:

$$\Omega_{\text{beat}} \simeq \Omega_s + \frac{\gamma \eta \Omega_s J_1^2(kx_m)}{T_1(\Omega_s^2 - \omega_m^2)} + \frac{\Re(\tilde{m}_1^{\,m} \tilde{m}_2^{\,m})}{2\Omega_s} + \frac{\Re(\tilde{m}_1^{\,c} \tilde{m}_2^{\,c}) \Omega_s J_1^2(kx_m)}{\Omega_s^2 - \omega_m^2} \tag{16}$$

Since the value of kx_m is deliberately chosen to be equal to the first zero of the J_0 function, the J_1 term becomes the dominant nonlinearity, with $J_1^2(kx_m) \simeq 0.27$. Eq. (16) is in good agreement with experimental data, as reported in Fig. 7, where the beat frequency is measured as a function of the pumping rate. The experimentally measured slope is -3.7 kHz, while the theoretical estimate from Eq. (16) leads to $-\gamma J_1^2(kx_m)\Omega_s/[2\pi T_1(\omega_m^2 - \Omega_s^2)] \simeq -3.6$ kHz (where we have used the following parameters: $\gamma = 15.34 \ 10^6 \ \text{s}^{-1}$, $\Omega_s/(2\pi) \simeq 117.3$ kHz, $T_1 = 230$ μs and $\omega_m/(2\pi) \simeq 168$ kHz).

Keeping only the leading order in the small quantity Ω_s/ω_m, the frequency shift induced by the parametric resonance described above can be rewritten as $-J_1^2(kx_m)[\omega_r/\omega_m]^2 \Omega_s$. In terms of gyroscope performance, this corresponds to a scale-factor nonlinearity, which is typically (with $\omega_r/(2\pi) \simeq 20$ kHz) on the order of 3×10^{-3}. With this parameters, this means in particular that the pumping rate η has to be controlled at the 10^{-3} level in order to make the scale factor stable at the ppm level. A similar control on the amplitude of the crystal vibration x_m is also required for the same reason. One way to relax the latter constraint would be to increase the vibration frequency f_m beyond its actual value of 168 kHz.
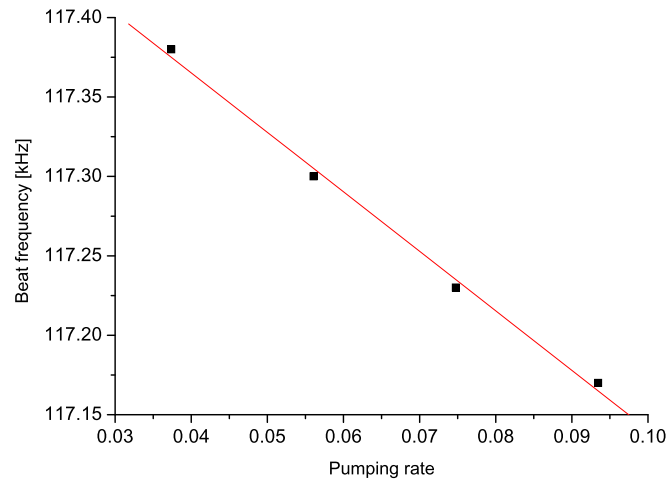
Fig. 7. Experimental frequency response of the solid-state ring laser gyroscope as a function of the pumping rate, with $J_0(kx_m) = 0$, $f_m \simeq 168$ kHz and $\dot{\theta} = 160$ deg/s. The measured slope is in good agreement with analytical predictions (Eq. (16)). (Color online.)
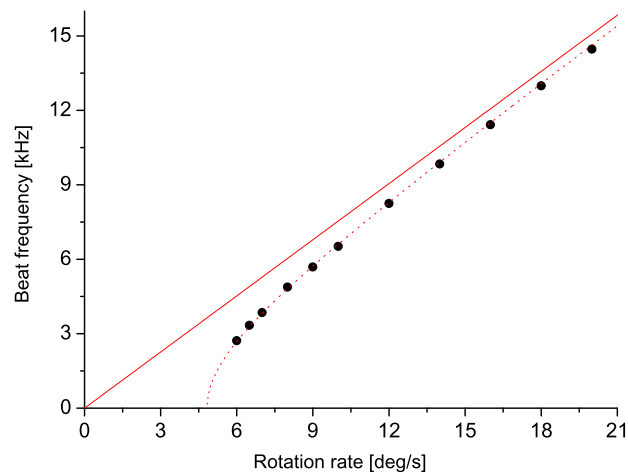

Fig. 8. Experimental frequency response of the solid-state ring laser gyroscope at low rotation rates, with $J_0(kx_m) = 0$ and $f_m \simeq 168$ kHz. The dashed line is a fit of the experimental data by the typical frequency response curve of a helium–neon RLG [27]. (Color online.)

4.3. Case of low rotation rates

When the condition $J_0(kx_m) = 0$ is fulfilled, the nonlinearity of the frequency response curve is significantly reduced, and the deviation from the ideal Sagnac line at low rotation rates is downwards, as illustrated in Fig. 8. It is a remarkable fact that the shape of this frequency response curve is now similar to what would be expected from a helium–neon RLG, where the dominant coupling source is (linear) backscattering on the cavity mirrors. This similarity is confirmed by the numerical simulations shown in Fig. 9, where the frequency response curve of a high-performance helium–neon RLG is shown to be identical to that of a solid-state RLG with the same mirror backscattering coefficients $\tilde{m}_{1,2}^m$. Further numerical simulations [32] including mechanical dither also show that the two devices are expected to have the same level of angular random walk if identical mirrors are used. In other words, everything happens at low rotation rates as if all sources of nonlinear coupling from the Nd–YAG crystal were effectively suppressed by the crystal vibration.

5. Conclusion

The ultimate level of performance that can be expected from the solid-state RLG (in addition to the scale factor effect outlined in the previous section) is discussed in Ref. [41]. As already mentioned, the angular random walk resulting from mechanical dither is expected to be the same as for a helium–neon RLG, provided mirrors of equivalent quality are used. The Schawlow–Townes limit [42] should be slightly higher in the case of the solid-state RLG because the finesse of the cavity is a little bit lower, although this will be partly compensated by the possibility to use more power thanks to the high gain in the Nd–YAG crystal. In total, the solid-state RLG should be able to reach the 10^{-3} deg/$\sqrt{h}$ range. As regards the
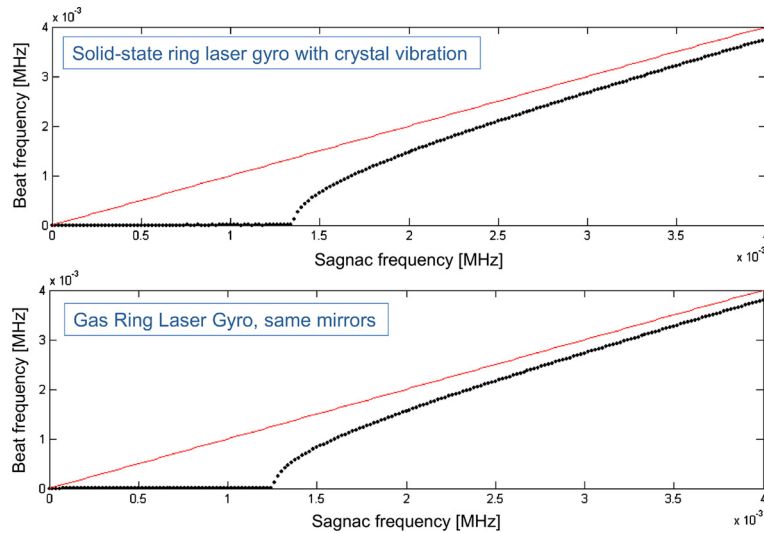
Fig. 9. Up: simulated frequency response curve of a solid-state RLG with crystal vibration at $f_m \simeq 168$ kHz and $J_0(kx_m) = 0$. All parameter values are taken from experimental measurements [38], except the mirror backscattering coefficients $\tilde{m}_{1,2}^m$, which have the typical value of a high-performance helium–neon RLG. Low: simulated frequency response curve of a high-performance helium–neon RLG (obtained by numerical integration of the Adler equation [27] with the same value of $\tilde{m}_{1,2}^m$ as for the upper curve). (Color online.)

ultimate bias stability, it is predicted to lay in the 10^{-2} deg/h range if the current flowing out of the feedback loop can be measured at the 10^{-3} level [41]. As discussed in this paper, the same precision will be required on the pumping rate and crystal vibration amplitude to reach the ppm level on the stability of the scale factor.

Experimental work is still ongoing at Thales to raise the Technology Readiness Level of the solid-state RLG (in particular by using high-quality mirrors at 1.064 µm and by improving the stability of the control electronics). Beyond industrial applications, this technology could also be an interesting platform to test more advanced schemes of rotation sensing, involving for example anomalous dispersion [14].

References

[1] G. Sagnac, L'éther lumineux démontré par l'effet du vent relatif d'éther dans un interféromètre en rotation uniforme, C. R. Acad. Sci. Paris 95 (1913) 708.
[2] G. Sagnac, Sur la preuve de la réalité de l'éther lumineux par l'expérience de l'interférographe tournant, C. R. Acad. Sci. Paris 95 (1913) 1410.
[3] W. Macek, D. Davis, Rotation rate sensing with traveling-wave ring lasers, Appl. Phys. Lett. 2 (3) (1963) 67.
[4] C. Ciminelli, F. Dell'Olio, C.E. Campanella, M.N. Armenise, Photonic technologies for angular velocity sensing, Adv. Opt. Photonics 2 (3) (2010) 370.
[5] H. Ma, Z. He, K. Hotate, Reduction of backscattering induced noise by carrier suppression in waveguide-type optical ring resonator gyro, J. Lightwave Technol. 29 (1) (2011) 85.
[6] H. Mao, H. Ma, Z. Jin, Polarization maintaining silica waveguide resonator optic gyro using double phase modulation technique, Opt. Express 19 (5) (2011) 4632.
[7] U. Leonhardt, P. Piwnicki, Ultrahigh sensitivity of slow-light gyroscope, Phys. Rev. A 62 (2000) 055801.
[8] A. Matsko, A. Savchenkov, V. Ilchenko, L. Maleki, Optical gyroscope with whispering gallery mode optical cavities, Opt. Commun. 233 (1) (2004) 107.
[9] B.Z. Steinberg, Rotating photonic crystals: a medium for compact optical gyroscopes, Phys. Rev. E 71 (5) (2005) 056621.
[10] J. Scheuer, A. Yariv, Sagnac effect in coupled-resonator slow-light waveguide structures, Phys. Rev. Lett. 96 (2006) 053901.
[11] B.Z. Steinberg, J. Scheuer, A. Boag, Rotation-induced superstructure in slow-light waveguides with mode-degeneracy: optical gyroscopes with exponential sensitivity, J. Opt. Soc. Am. B 24 (5) (2007) 1216.
[12] M.S. Shahriar, G.S. Pati, R. Tripathi, V. Gopal, M. Messall, K. Salit, Ultrahigh enhancement in absolute and relative rotation sensing using fast and slow light, Phys. Rev. A 75 (2007) 053807.
[13] M. Salit, G. Pati, K. Salit, M. Shahriar, Fast-light for astrophysics: super-sensitive gyroscopes and gravitational wave detectors, J. Mod. Opt. 54 (16–17) (2007) 2425.
[14] S. Schwartz, F. Goldfarb, F. Bretenaker, Some considerations on slow-and fast-light gyros, Opt. Eng. 53 (10) (2014) 102706.
[15] H.K. Kim, M.J. Digonnet, G.S. Kino, Air-core photonic-bandgap fiber-optic gyroscope, J. Lightwave Technol. 24 (8) (2006) 3169.
[16] G.A. Sanders, L.K. Strandjord, T. Qiu, Hollow core fiber optic ring resonator for rotation sensing, in: Optical Fiber Sensors, Optical Society of America, 2006, p. ME6.
[17] M.A. Terrel, M.J. Digonnet, S. Fan, Resonant fiber optic gyroscope using an air-core fiber, J. Lightwave Technol. 30 (7) (2012) 931.
[18] K. Schreiber, T. Klügel, J.-P. Wells, R. Hurst, A. Gebauer, How to detect the Chandler and the annual wobble of the Earth with a large ring laser gyroscope, Phys. Rev. Lett. 107 (17) (2011) 173904.
[19] F. Bosi, G. Cella, A. Di Virgilio, A. Ortolan, A. Porzio, S. Solimeno, M. Cerdonio, J. Zendri, M. Allegrini, J. Belfi, et al., Measuring gravitomagnetic effects by a multi-ring-laser gyroscope, Phys. Rev. D 84 (12) (2011) 122002.
[20] K. Schreiber, A. Gebauer, J.-P. Wells, Long-term frequency stabilization of a 16 m^2 ring laser gyroscope, Opt. Lett. 37 (11) (2012) 1925.
[21] C. Clivati, D. Calonico, G.A. Costanzo, A. Mura, M. Pizzocaro, F. Levi, Large-area fiber-optic gyroscope on a multiplexed fiber network, Opt. Lett. 38 (7) (2013) 1092.
[22] W. Chow, J. Gea-Banacloche, L. Pedrotti, V. Sanders, W. Schleich, M. Scully, The ring laser gyro, Rev. Mod. Phys. 57 (1) (1985) 61.
[23] H. Lefèvre, The Fiber-Optic Gyroscope, Artech House, 1993.

[24] J. Gea-Banacloche, Passive versus active interferometers: why cavity losses make them equivalent, Phys. Rev. A 35 (6) (1987) 2518.
[25] D.M. Shupe, Thermally induced nonreciprocity in the fiber-optic interferometer, Appl. Opt. 19 (5) (1980) 654.
[26] J. Killpatrick, The laser gyro, IEEE Spectr. 4 (10) (1967) 44.
[27] F. Aronowitz, Fundamentals of the ring laser gyro, in: Optical Gyros and Their Application, NATO Research and Technology Organization, 1999 (Ch. 3).
[28] A. Dotsenko, E. Lariontsev, Use of a feedback circuit for the improvement of the characteristics of a solid-state ring laser, Sov. J. Quantum Electron. 14 (1) (1984) 117.
[29] A. Dotsenko, L.S. Kornienko, N.V. Kravtsov, E. Lariontsev, O. Nanii, A. Shelaev, Use of a feedback loop for the stabilization of a beat regime in a solid-state ring laser, Sov. J. Quantum Electron. 16 (1) (1986) 58.
[30] S. Schwartz, G. Feugnet, P. Bouyer, E. Lariontsev, A. Aspect, J.-P. Pocholle, Mode-coupling control in resonant devices: application to solid-state ring lasers, Phys. Rev. Lett. 97 (2006) 093902.
[31] S. Schwartz, F. Gutty, J.-P. Pocholle, G. Feugnet, Solid-state ring laser gyro with a mechanically activated gain medium, US Patent 7,589,841.
[32] S. Schwartz, F. Gutty, G. Feugnet, E. Loil, J.-P. Pocholle, Solid-state ring laser gyro behaving like its helium–neon counterpart at low rotation rates, Opt. Lett. 34 (24) (2009) 3884.
[33] H. Danielmeyer, E. Turner, Electro-optic elimination of spatial hole burning in lasers, Appl. Phys. Lett. 17 (12) (1970) 519.
[34] H. Danielmeyer, W. Nilsen, Spontaneous single-frequency output from a spatially homogeneous Nd–YAG laser, Appl. Phys. Lett. 16 (3) (1969) 124.
[35] S. Schwartz, F. Gutty, G. Feugnet, P. Bouyer, J.-P. Pocholle, Suppression of nonlinear interactions in resonant macroscopic quantum devices: the example of the solid-state ring laser gyroscope, Phys. Rev. Lett. 100 (2008) 183901.
[36] E.J. Post, Sagnac effect, Rev. Mod. Phys. 39 (2) (1967) 475.
[37] H.R. Bilger, W.K. Stowell, Light drag in a ring laser: an improved determination of the drag coefficient, Phys. Rev. A 16 (1977) 313.
[38] S. Schwartz, G. Feugnet, E. Lariontsev, J.-P. Pocholle, Oscillation regimes of a solid-state ring laser with active beat-note stabilization: from a chaotic device to a ring-laser gyroscope, Phys. Rev. A 76 (2) (2007) 023807.
[39] J. Kevorkian, J. Cole, Multiple Scale and Singular Perturbation Methods, Springer, 1996.
[40] J. Sanders, F. Verhulst, J. Murdock, Averaging Methods in Nonlinear Dynamical Systems, Springer, 2007.
[41] S. Schwartz, F. Gutty, G. Feugnet, J.-P. Pocholle, Performance evaluation of a solid-state ring laser gyro, in: Proceedings of the Symposium Gyro Technology, Karlsruhe, Germany, 2010.
[42] T. Dorschner, H. Haus, M. Holz, I. Smith, H. Statz, Laser gyro at quantum limit, IEEE J. Quantum Electron. 16 (12) (1980) 1376.